Role of Trichocytic Keratins in Anti-Neuroinflammatory Effects After Spinal Cord Injury

Wenjie Zhong, Dongjie Shi, Junjie Zhou, Yaying Yang, Bochu Wang, Xiaochuan Sun, Qian Shu, Wenfeng Li, Yongzhi Xia, Lei Ao, KangLin Xiong, Shilei Hao,* and Haijian Xia*

Shifting microglia/macrophages to M2 anti-inflammatory phenotype is considered a pivotal therapeutic target for spinal cord injury (SCI). Keratin extracted from human hair exhibits anti-inflammatory properties. However, the differences among the 17 types of human hair keratins and their mechanisms of anti-inflammation remain poorly understood. In this study, the anti-inflammatory activity of 17 human hair keratins using a recombinant synthesis approach is explored. Distinct activities of microglia/macrophage phenotype modulation of 17 keratins are found through qRT-PCR analysis, and recombinant keratin 33A (RK33A) and RK35 display superior anti-inflammatory efficiency compared to other keratins. Immunofluorescence and flow cytometry reveals a significant effect of RK33A on the regulation of microglia/macrophages into an anti-inflammatory M2 phenotype. Subsequently, recombinant keratin 33A nanofiber (RKNF33A) is fabricated to evaluate its in vivo anti-inflammatory and nerve regeneration properties using the rat T9 spinal cord lateral hemisection model. The optimized keratin-based nanofiber shows outstanding performance in enhancing M2 polarization, reducing glial scarring, promoting nerve regeneration, and improving locomotor function recovery in SCI rats. Moreover, it is preliminarily found that RK33A regulates M2 microglia/macrophage polarization by upregulating the PI3K/AKT/mTOR signaling pathway. Together, this study reveals that trichocytic keratins exhibit distinct anti-inflammatory properties, providing a prospective treatment for SCI by modulating microglia/macrophage polarization.

1. Introduction

Spinal cord injury (SCI) is a severe neurological disorder that leads to loss of motor function and many essential complications.[1] After SCI, the primary injury caused by the initial trauma leads to neuronal death and neural tissue necrosis.[2] The secondary injury cascade starts a few minutes after injury and can cause serious hemorrhage, edema, neuroinflammation, and neuronal tissue loss.[3] Neuroinflammation is one of the main pathogeneses of secondary injury due to the rapid infiltration of M1 ("classically activated") microglia/macrophages, which secrete pro-inflammatory cytokines to facilitate neuronal apoptosis and aggravate secondary injury.[4] In contrast, M2 ("alternatively activated") microglia/macrophages infiltrate only transiently and in small numbers and release anti-inflammatory factors against inflammation, promoting tissue regeneration.[5,6] These immune cells exist on a continuum between two different polarized phenotypes.[7] Therefore, augmenting the polarization of microglia/macrophages from the pro-inflammatory M1 phenotype to the anti-inflammatory M2 phenotype is a promising strategy for SCI treatment.

Substantial efforts have been aimed at regenerative therapies that may promote neuronal repair and establish connectivity across the injury site. Tissue engineering scaffolds made of biomaterials have been used to support nerve cells in the injured spinal cord.[8,9] Aligned electrospun nanofibers have attracted considerable attention owing to their unique properties, such as the contact guidance effect, which has been proven to guide longer regenerated neurites across the lesion gap.[10–13] However, despite the considerable success achieved with many biomaterials in rats, including collagen[14] and chitosan,[15] there is still a lack of ideal biomaterials for the clinical repair of SCI. Therefore, considering the hostile pro-inflammatory microenvironment after SCI,[16] finding a neural-friendly biomaterial that can regulate the microglia/macrophage phenotype shift to ameliorate the inflammatory response and provide a sustained neurogenic microenvironment after SCI remains challenging.

W. Zhong, D. Shi, X. Sun, Y. Xia, L. Ao, K. Xiong, H. Xia
Department of Neurosurgery
The First Affiliated Hospital of Chongqing Medical University
Chongqing 400016, China
E-mail: 202479@cqmu.edu.cn

J. Zhou, Y. Yang, Q. Shu
Department of Pathology
Molecular Medicine and Tumor Center
Chongqing Medical University
Chongqing 400016, China

B. Wang, W. Li, S. Hao
Key Laboratory of Biorheological Science and Technology
Ministry of Education, College of Bioengineering
Chongqing University
Chongqing 400030, China
E-mail: shilei_hao@cqu.edu.cn

Human hair keratins have been proven to be excellent biomaterials owing to their biocompatibility, biodegradability, and natural abundance[17] and have been used in biomedical applications.[18–20] In our previous study, human hair keratins demonstrated strong effects on hemostasis[20,21] and wound healing.[22] In addition, it has been reported that human hair keratins could convert macrophages into the M2 anti-inflammatory phenotype in vitro,[23,24] suggesting the potential value to further investigate their anti-inflammatory mechanisms. However, extracted human hair keratins have complex components, such as keratin, keratin-associated, and intermediate filament proteins. Additionally, the characteristics of extracted keratins are difficult to control because of the use of numerous extraction methods and varied sources of raw materials.[25] It is almost impossible to investigate an individual type or component of the extracted keratins.[26] Therefore, recombinant expression provides a reliable way to evaluate the immunomodulatory effects of each type of keratin.[27] According to our previous study, recombinant trichocytic keratins (RKs) display higher purity, more stable characteristics, and excellent biocompatibility.[25,28] A few RKs have demonstrated stronger effects on halting bleeding[28] and wound healing[25] than extracted keratins. Therefore, it is of great translational value to observe and select the most valuable type of RKs for the microglia/macrophage phenotype shift.

In this study, we expressed and purified 17 RKs and evaluated their effects on microglia/macrophage polarization. Subsequently, we fabricated recombinant keratin nanofibers (RKNFs) and established a rat T9 spinal cord lateral hemisection model to assess their therapeutic effects on inflammation, nerve regeneration, and locomotor function. Furthermore, we investigated this intrinsic mechanism in vitro.

2. Results

2.1. RKs Expression and Characterization

There was 11 acidic type I family and six neutral-basic type II family trichocytic keratin proteins (**Figure 1**A), and all 17 RKs were well-expressed in the *Escherichia coli* system. All RKs were obtained in inclusion bodies with yields of ≈40–60 mg L^{-1} and were further purified using Ni-column to isolate a single protein. Sodium dodecyl sulfate-polyacrylamide gel electrophoresis (SDS-PAGE) analysis revealed that the molecular weight of purified RKs ranged from 45–65 kDa, and all were purified showing single bands (Figure S1, Supporting Information) that correlated with their respective molecular weights (Table S1, Supporting Information), indicating excellent purity of RKs compared to previous keratins extracted from human hair.

Circular dichroism (CD) analysis was performed to determine the secondary structures of purified RKs (Figure 1B). All RKs exhibited characteristic α-helical spectra with negative minimum absorption peaks at 208 and 222 nm. Although different RKs showed slightly shifted minima CD spectra, their overall shapes were similar.

Furthermore, we performed Fourier transform infrared spectroscopy (FT-IR) analysis in the region of 400–5000 cm^{-1} (Figure 1C) to reveal the chemical structures of purified RKs. Characteristic amide bands were detected that correlated with the peptide linkage in the spectra at 3300 cm^{-1} (N–H stretching vibrations, amide A), 1700–1600 cm^{-1} (C–O stretching, amide I), 1540–1520 cm^{-1} (N–H bending and C–H stretching vibrations, amide II), and 1220–1300 cm^{-1} (C–N stretching and C–O bending vibrations, amide III).
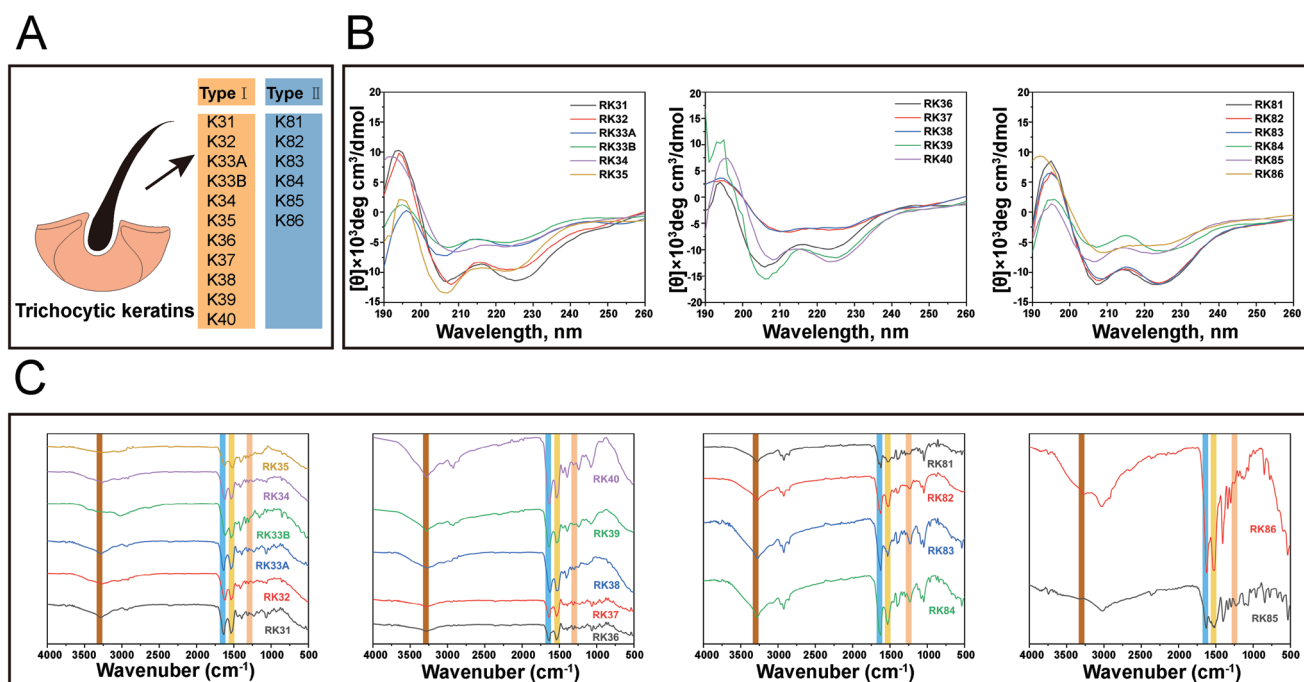

Figure 1. Physicochemical properties of 17 RKs. A) Trichocytic keratins include 11 acidic types I family and six neutral-basic type II family. The CD spectra B) and FT-IR spectra C) of RKs. RKs, recombinant trichocytic keratins; CD, circular dichroism; FT-IR, Fourier transform IR.

2.2. Effects of RKs on Microglia Polarization in BV2 Cells

The in vitro cytotoxicity of the RKs was evaluated using CCK-8 and LIVE/DEAD viability/cytotoxicity assays. CCK-8 analysis demonstrated no significant differences between different types of RKs in terms of overall cell viability (Figure S2A, Supporting Information). The LIVE/DEAD assay showed the presence of a few dead cells (red stain cells) (Figure S2B, Supporting Information). These results indicated that RKs preserved superior cytocompatibility.

To investigate the different effects of RKs on microglial polarization, we examined the mRNA expression of M1- (IL-1β, iNOS, and TNF-α) (**Figure 2**A) and M2- (Mrc1, Arg1, CD163, and IL-10) related genes (Figure 2B) in BV2 cells using qPCR after LPS and IFN-γ (shortened as LPS) stimulation with or without RKs for 24 h. We found that 17 RKs had heterogeneous effects on gene regulation; a few RKs down-regulated the relative gene expression of M1, whereas a few other RKs upregulated M2 gene expression. These results demonstrated a potentially beneficial immune regulation for resolving inflammation after SCI. Intriguingly, RK35 and RK33A reduced the expression of M1-related genes (Figure 2A, $p < 0.01$) and reversed the decreased expression of M2-related genes (Figure 2B, $p < 0.05$), suggesting that these RKs may play a role in shifting M1 microglia to M2 microglia. RK83, which exhibited no effect, was selected along with RK35 and RK33A for further experiments.

To further evaluate the effects of RK83, RK35, and RK33A on CD86 (M1 surface marker) (Figure 2C) and CD206 (M2 surface marker) (Figure 2D), immunofluorescence (IF) staining analysis was performed. We found that RK35 and RK33A reduced CD86$^+$ cells (Figure 2E, $p < 0.01$) and increased CD206$^+$ cells (Figure 2F, $p < 0.001$), respectively, under LPS stimulation. RK33A showed a better influence on the M2 polarization of BV2 cells than that of RK35 (Figure 2E,F, $p < 0.05$). RK83 showed no significant difference (Figure 2E,F), as determined by qPCR (Figure 2A,B). Furthermore, flow cytometry analysis confirmed that RK33A noticeably decreased the expression of CD86 (Figure 2G,I, $p < 0.05$) and increased the expression of CD206 (Figure 2H,J, $p < 0.0001$) in LPS-stimulated BV2 cells; the effects were superior to those of RK35 (Figure 2H,J, $p < 0.05$).

2.3. Fabrication and Characterization of RKNFs

To evaluate in vivo anti-inflammatory and nerve regeneration properties of RKs, we fabricated polycaprolactone (PCL) nanofibers, recombinant keratin 83 nanofibers (RKNF83), RKNF35, and RKNF33A based on our cell experiment results using electrospinning (**Figure 3**A; Figure S3A, Supporting Information) and observed the morphologies of nanofibers using scanning electron microscopy (SEM). The PCL nanofiber and RKNFs presented with an aligned distribution in the high-rotation-speed settings (Figure 3B). Furthermore, when 100 nanofibers were randomly selected, nanofiber diameters were found to be in the range of 100–400 nm (Figure 3B).

To observe the chemical structure of the nanofibers, FT-IR analysis was performed in the region of 400–5000 cm^{-1}. Both PCL-related characteristic peaks at 2930 cm^{-1} (asymmetric CH^2 stretching) and 2860 cm^{-1} (symmetric CH^2 stretching) and keratin-related characteristic peaks (as previously described) were observed in the RKNFs (Figure 3C), verifying the successful combination of RKs and PCL.

The hydrophilicity of biomaterials significantly affected their biocompatibility, which was one of the most important elements in tissue engineering.[29] We employed water contact angle measurement (Figure 3D). The water contact angles of RKNF83 ($\approx 56°$), RKNF35 ($\approx 50°$), and RKNF33A ($\approx 53°$) were significantly lower than those of the PCL nanofibers ($\approx 84°$) (Figure 3D, $p < 0.0001$), indicating that the combination with RKs enhanced the hydrophilicity of PCL and is expected to exhibit better affinity for tissues. Notably, proper mechanical properties are required for the preservation of the biomaterial scaffold, owing to the physiology of the spine.[30] The tensile strength of all nanofiber scaffolds ranged from 2–4 MPa (Figure 3E). Owing to the existence of RKs, RKNFs seemed to have better elongation (Figure 3E), suggesting that the durability and flexibility of RKNFs were improved compared to PCL nanofibers, with slightly decreased tensile strength.

2.4. RKNFs Promoted Locomotor Function Recovery After SCI In Vivo

To evaluate the effect of RKNFs in vivo, a rat T9 spinal cord lateral hemisection model was implanted with PCL nanofibers (PCL group), RKNF83 (RKNF83 group), RKNF35 (RKNF35 group), and RKNF33A (RKNF33A group). The SCI group of animals was not implanted (**Figure 4**A,B). Basso, Beattie, and Bresnahan (BBB) locomotor score behavioral assessment was performed to evaluate the hindlimb function of the rats at 1, 3 d, 1, 2, 3, 4, and 8 weeks post-injury (wpi) (Video S1, Supporting Information). The RKNF33A group showed a better locomotor functional recovery than that of the SCI, PCL, RKNF83, and RKNF35 groups (Figure 4C, $p < 0.0001$).

The open field test was performed at 4 and 8 weeks after SCI. The rats in the RKNF33A group demonstrated more movements all over the field (center as well as periphery), whereas rats in other groups mostly stayed at the corner or moved around the periphery of the field (Figure 4D). In the footprint analysis performed at 4 and 8 wpi to visually observe right hind limb recovery, rats in the RKNF33A group exhibited improved locomotor coordination with longer stride length (Figure 4E, $p < 0.05$) and clearer right footprints (Figure 4F,G) than those in other groups. Animals in SCI, PCL, RKNF83, and RKNF35 groups showed shorter stride lengths (Figure 4E, $p < 0.05$) and dragged right hind limb footprints (Figure 4F,G).

When 15 rats were sacrificed at 1 and 8 wpi to explore the histological structures of regenerated tissues, at both time points, visible cavities at the lesion sites appeared smaller in the RKNF33A group than that in the other four groups (Figure S3B,C, Supporting Information). Moreover, at 1 and 8 wpi, hematoxylin and eosin (HE) and Luxol Fast Blue (LFB) staining procedures performed to observe the general shapes and pathological changes in the injured spinal cord revealed tissue-filled lesion sites and increased myelin sparring, respectively, in the RKNF33A group in comparison to other groups (Figure 4H,I).
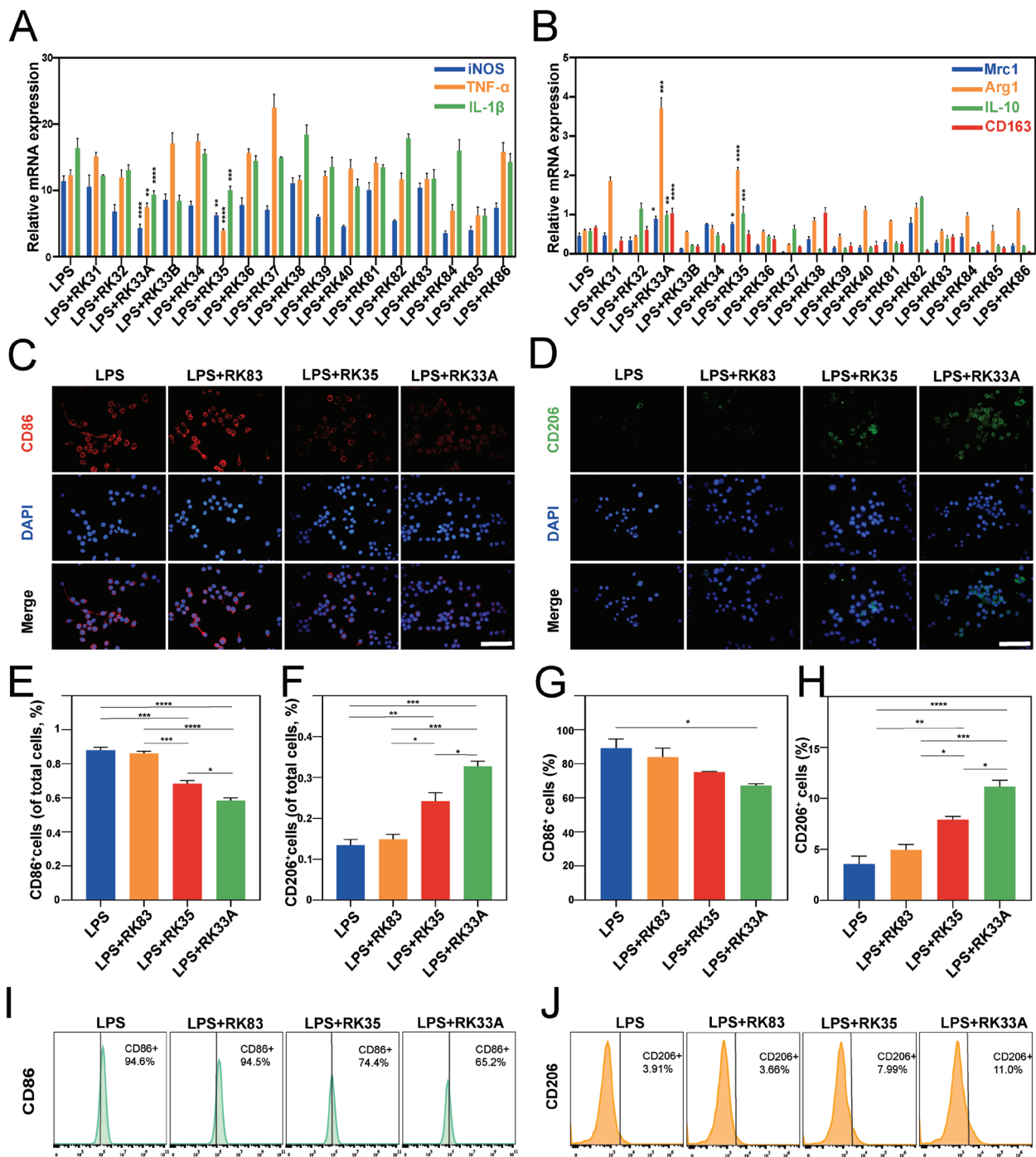
Figure 2. Heterogeneous effects of different RKs on the polarization of BV2 microglial cells after 24 h LPS stimulation. Expression of M1 (iNOS, TNF-α, and IL-1β) A) and M2 (Mrc1, Arg1, IL-10, and CD163) B) related genes were assessed using qRT-PCR. C–F) Representative images and quantitative analysis of CD86 (red) and CD206 (green) immunofluorescent staining BV2 cells. Cell nuclei were co-stained with DAPI (blue). G–J) Representative flow cytometry histograms and quantitative analysis of CD86$^+$ and CD206$^+$ BV2 cells. All data represented the mean ± standard error of mean and were calculated using ANOVA, $n = 3$, $*p < 0.05$, $**p < 0.01$, $***p < 0.001$, $****p < 0.0001$. Scale bar: 100 µm. LPS, LPS and IFN-γ.

2.5. RKNFs Promoted Nerve Regeneration and Reduced the Glia Scar After SCI In Vivo

Immunofluorescence staining performed at the lesion epicenter 8 weeks after SCI showed decreased glial fibrillary acidic protein (GFAP) expression in the RKNF33A group compared with the other four groups (**Figure 5**A,D, $p < 0.0001$), suggesting alleviation of glial scar at 8 wpi. When tissue samples were stained with β-tubulin III (newborn neurons) (Figure 5B) and neurofilament-200 (NF200, mature neurons)

**ADVANCED
SCIENCE NEWS**

www.advancedsciencenews.com

**ADVANCED
FUNCTIONAL
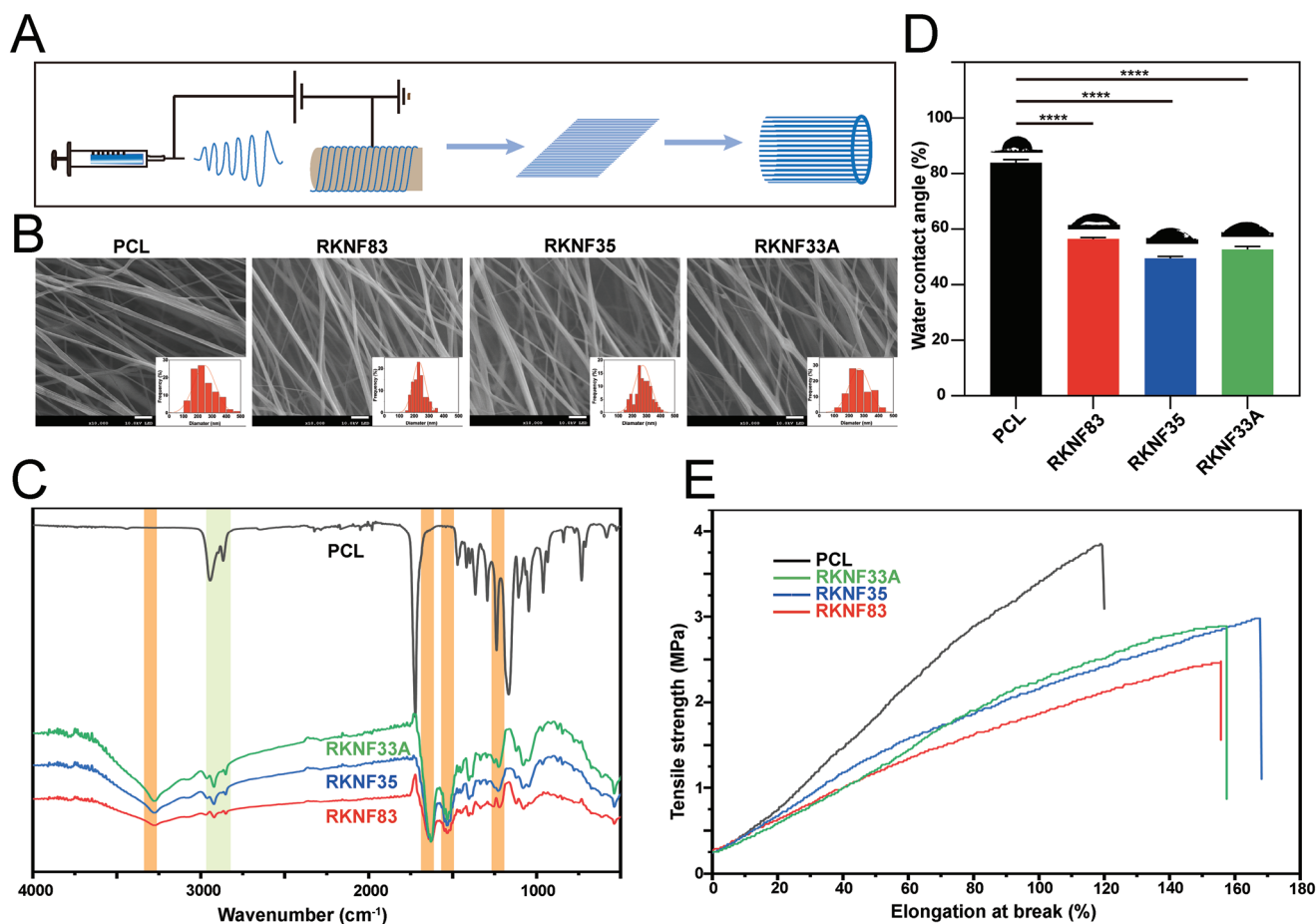MATERIALS**

www.afm-journal.de

Figure 3. Characterization of RKNFs. A) Schematic illustration of the electrospinning process. B) SEM morphologies of aligned PCL nanofibers and RKNFs. The histogram at the right-bottom corner of each panel shows the corresponding diameter distributions of the nanofibers. Scale bar: 1 µm. The FT-IR spectra C), the optical pictures and quantitative analysis of water contact angles D), and the mechanical properties E) of PCL nanofibers and RKNFs. All data represented the mean ± standard error of mean and were calculated using ANOVA, $n = 3$, *$p < 0.05$, **$p < 0.01$, ***$p < 0.001$, ****$p < 0.0001$. RKNFs, recombinant keratin nanofibers; SEM, scanning electron microscopy.

(Figure 5C), in comparison to SCI, PCL, and RKNF83 groups, more β-tubulin III$^+$ (Figure 5D, $p < 0.0001$) and NF200$^+$ cells (Figure 5D, $p < 0.05$) were detected in the RKNF33A group. The RKNF33A group also showed more β-tubulin III$^+$ cells than the RKNF35 group (Figure 5D, $p < 0.05$).

2.6. RKNFs Regulated M2 Polarization of Microglia/Macrophage After SCI In Vivo

To evaluate the performance of RKNFs in augmenting the polarization of microglia/macrophages after SCI, CD86 (**Figure 6**A,B) and CD206 (Figure 6C,D), representing M1 and M2 microglia/macrophages, respectively, were detected by IF staining at the lesion epicenters at 1 and 8 wpi. The RKNF33A group showed a reduction in CD86$^+$/Iba1$^+$ compared with the other four groups (Figure 6E,F, $p < 0.05$). More CD206$^+$/Iba1$^+$ cell infiltration was observed in the RKNF33A groups, whereas SCI, PCL, RKNF83, and RKNF35 groups exhibited limited CD206$^+$/Iba1$^+$ expression at both time points (Figure 6G,H, $p < 0.05$). These results suggest that RKNF33A has a long-term

effect on recruiting more M2 microglia/macrophages at lesion sites. Enzyme-linked immunosorbent assay (ELISA) was performed to measure the levels of TNF-α and IL-10 in the serum of rats at 1 and 8 wpi. In comparison to other groups, the RKNF33A group had inhibited levels of TNF-α (Figure 6I,J, $p < 0.05$) and stimulated secretion of IL-10 (Figure 6K,L, $p < 0.05$), suggesting long-term alleviation of inflammation. These results indicate RKNF33A-promoted polarization of microglia/macrophages from M1 to M2 phenotype.

2.7. RK33A Induced M2 Polarization by Activating the PI3K/AKT/mTOR Signaling Pathway In Vitro

To further investigate the possible mechanism of microglia/macrophage polarization by RKs, we measured the expression levels of proteins of the PI3K/AKT/mTOR signaling pathway in BV2 microglia cells after LPS stimulation with or without RKs for 24 h (**Figure 7**A). LPS stimulation markedly decreased the ratios of p-PI3K/PI3K (Figure 7B, $p < 0.01$), p-AKT/AKT (Figure 7C, $p < 0.05$), and p-mTOR/mTOR (Figure 7D,
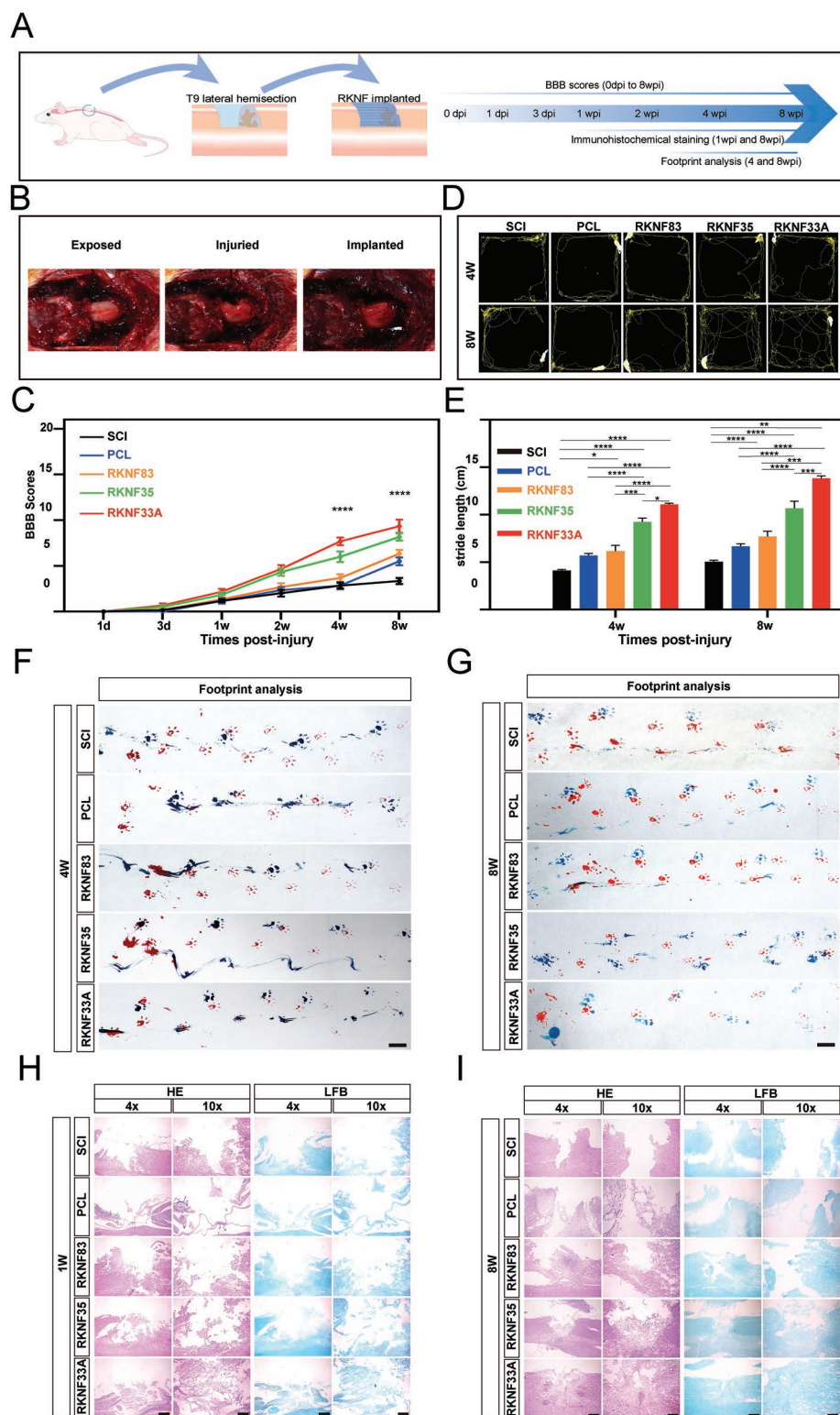
Figure 4. RKNF33A implantation promoted locomotor function after SCI. A) Schematic illustrating in vivo experimental design. B) A 2 mm hemisection was performed on the right side of the rat T9 spinal cord, and the nanofiber was implanted. C) Quantitative assessment of hind limb locomotor function using BBB scores at 1, 3 d, 1, 2, 3, 4 weeks, and 8 wpi. D) Representative images of the open field test at 4 and 8 wpi. Yellow trials represent the movements of the rats inside the open field. E) The stride length of rat hindlimbs in the footprint analysis at 4 and 8 wpi. F,G) Representative images of footprints from the different groups at 4 and 8 wpi. Forelimb footprints are shown in red, and hindlimb footprints are shown in blue. Scale bar: 1 cm. H,I) HE and LFB staining of the spinal cord tissues at different magnifications at 1 and 8 wpi. Scale bars:500 µm (4x) and 200 µm (10x). SCI, spinal cord injury; BBB, Basso, Beattie, and Bresnahan; wpi, weeks post-injury; HE, hematoxylin and eosin; LFB, Luxol Fast Blue. All data represented the mean ± standard error of the mean and were calculated using ANOVA, $n = 3$, *$p < 0.05$, **$p < 0.01$, ***$p < 0.001$, ****$p < 0.0001$.

**ADVANCED
SCIENCE NEWS**

www.advancedsciencenews.com

**ADVANCED
FUNCTIONAL
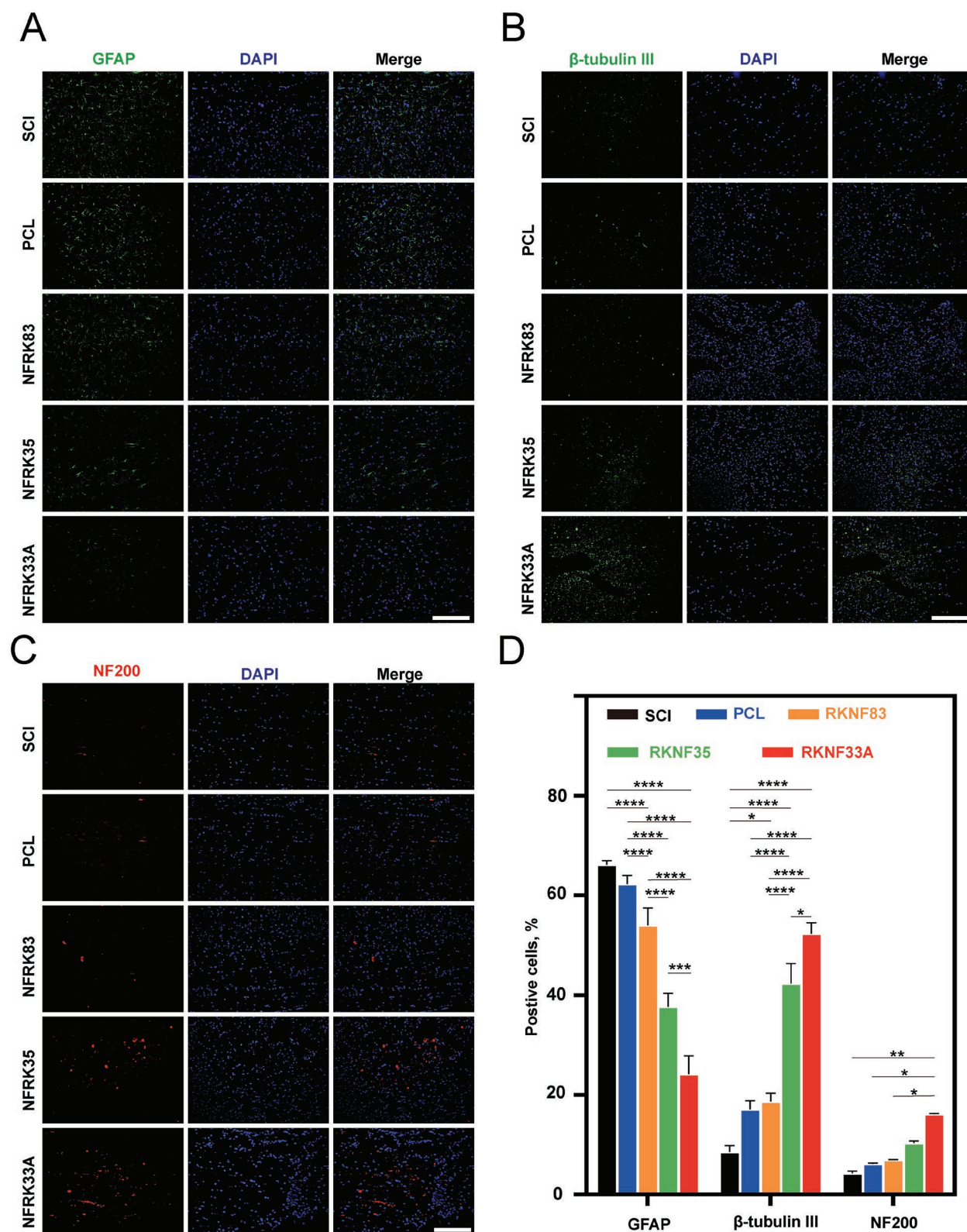MATERIALS**

www.afm-journal.de

Figure 5. RKNF33A implantation promoted axonal regeneration and reduced scar formation after SCI. Representative images of immunofluorescence staining of GFAP (green) A), β-tubulin III(green) B), and NF200 (red) C) at lesion epicenters in different nanofibers treatments at 8 wpi. Cell nuclei were co-stained with DAPI (blue). D) Quantitative analysis of GFAP[+], NF200^{+}, and β-tubulin III^{+} cells in (A, B, and C). All data represented the mean ± standard error of mean and were calculated using ANOVA, $n = 3$, *$p < 0.05$, **$p < 0.01$, ***$p < 0.001$, ****$p < 0.0001$. Scale bar: 200 µm. GFAP, glial fibrillary acidic protein; NF200, neurofilament 200.

**ADVANCED
SCIENCE NEWS**

www.advancedsciencenews.com

**ADVANCED
FUNCTIONAL
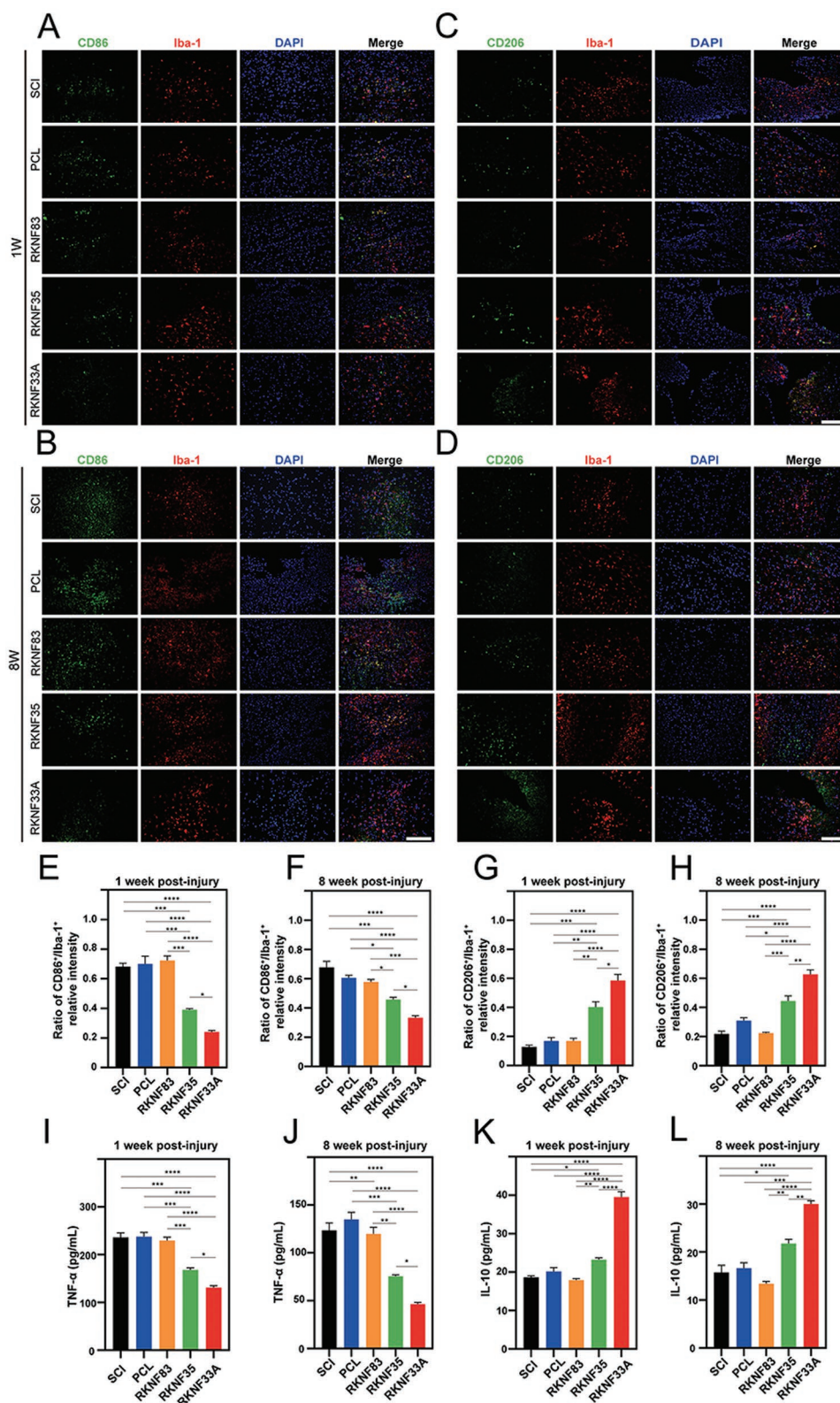MATERIALS**

www.afm-journal.de

Figure 6. RKNF33A implantation regulated the phenotype shift of microglia/macrophages in vivo. Representative image of CD86 (green)/Iba-1 (red) A,B) and CD206 (green)/Iba-1 C,D) immunofluorescence staining of different groups at lesion epicenters at 1 and 8 wpi. Cell nuclei were co-stained with DAPI (blue). E–H) Quantitative analysis of $CD86^+/Iba-1^+$ and $CD206^+/Iba-1^+$ cells in (A, B, C, and D). The level of pro-inflammatory TNF-α I,J) and anti-inflammatory cytokines IL-10 K,L) in the serum of rats at 1 and 8 wpi were measured by ELISA. All data represented the mean ± standard error of mean and were calculated using ANOVA, $n = 3$, *$p < 0.05$, **$p < 0.01$, ***$p < 0.001$, ****$p < 0.0001$. Scale bar: 200 µm.

**ADVANCED
SCIENCE NEWS**

www.advancedsciencenews.com

**ADVANCED
FUNCTIONAL
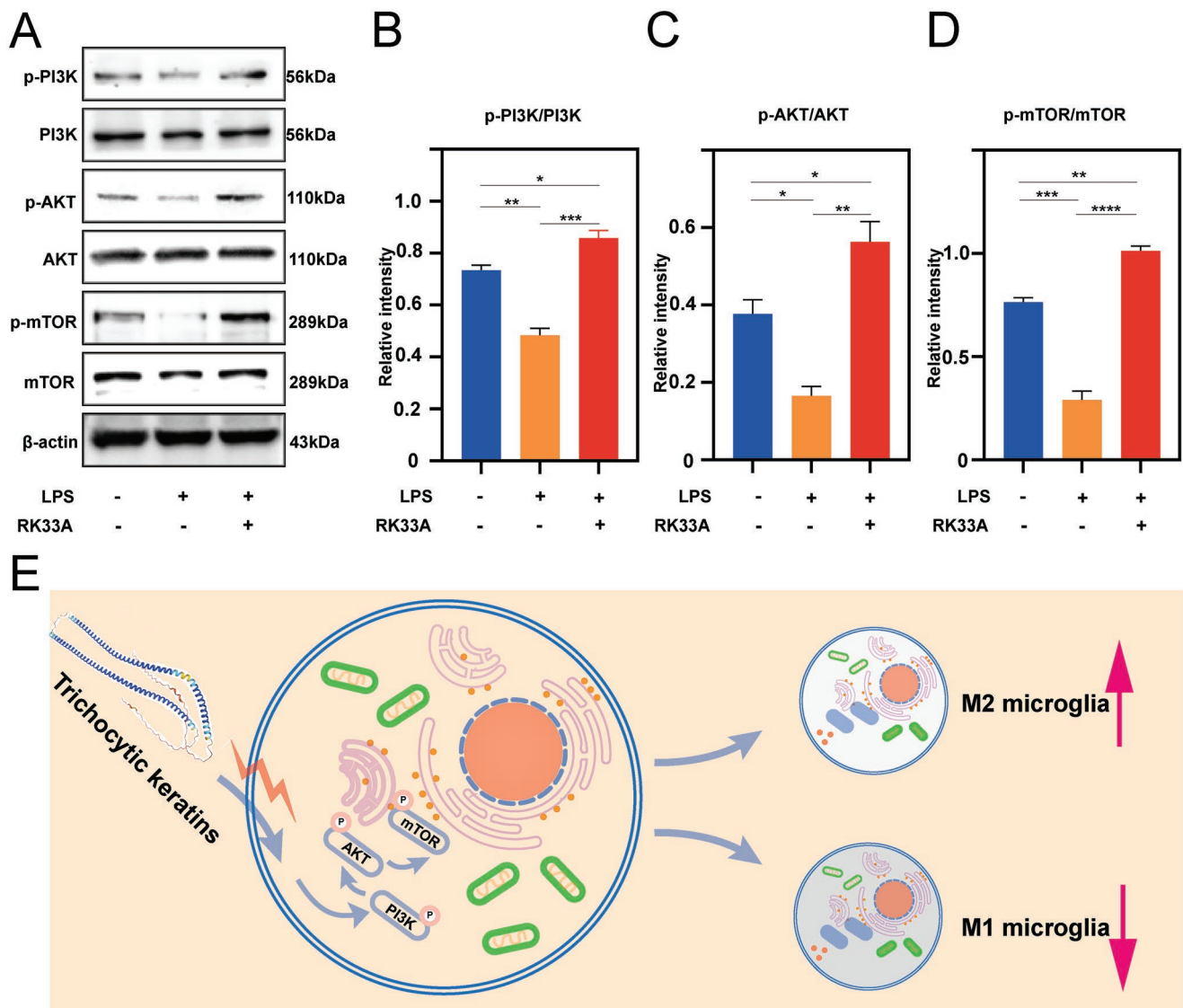MATERIALS**

www.afm-journal.de

Figure 7. RK33A regulated the M2 polarization of microglia by activating the PI3K/AKT/mTOR signaling pathway in vitro. A) Representative western blot showing the levels of PI3K, AKT, mTOR, and the phosphorylated proteins in BV2 cells after the stimulation of LPS with or without RK33A for 24 h. B–D) Quantitative analysis of p-PI3K/PI3K, p-AKT/AKT, and p-mTOR/mTOR ratios in (A). E) Schematic illustration of the intrinsic mechanism of trichocytic keratins for M2 microglia regulation. All data represented the mean ± standard error of mean and were calculated using ANOVA, $n = 3$, $*p < 0.05$, $**p < 0.01$, $***p < 0.001$, $****p < 0.0001$.

$p < 0.001$). The addition of RK33A reversed this trend and up-regulated the relative levels of p-PI3K/PI3K (Figure 7B, $p < 0.05$), p-AKT/AKT (Figure 7C, $p < 0.01$), and p-mTOR/mTOR (Figure 7D, $p < 0.0001$). These results revealed that RK33A regulated M2 polarization of BV2 cells, at least partially, via the PI3K/AKT/mTOR pathway (Figure 7E).

3. Discussion

Neuroinflammation is the most severe secondary damage in several brain diseases, including craniocerebral trauma, intracerebral hemorrhage, and SCI, which directly or indirectly impairs nerve regeneration and controls post-injury

sequelae.[4,31–33] Ameliorating the pro-inflammatory microenvironment has become a major therapeutic target for reducing secondary cell death and facilitating neuronal regeneration after SCI.[4] This is the first study to highlight the ability of RKs to influence the phenotype of microglia and evaluate their differential immunoregulatory and restorative effects as implantable bridging scaffolds in vivo after SCI.

Here, we explored the anti-inflammatory effects of 17 RKs and demonstrated that they are capable of switching microglial phenotypes in the absence of exogenously administered cytokines. Interestingly, the effects of different RKs on LPS-stimulated microglia were heterogeneous. We found that RK35 and RK33A inhibited the expression of M1-related genes and induced the expression of M2-related genes. It was also

ADVANCED
SCIENCE NEWS
www.advancedsciencenews.com

ADVANCED
FUNCTIONAL
MATERIALS
www.afm-journal.de

confirmed that RK33A is the most valuable subtype of human hair keratins in the M2 adoptive transfer of microglia. Taken together, these results provide sufficient evidence to further extend the development of keratin-based biomaterials.

Despite their unique structures and properties, the relatively brittle mechanical properties of RKs hinder scaffold fabrication. Through our exploration, blending PCL with RKs (8/2 w/w) is an alternative method for fabricating RKNFs. The results revealed that RKNFs had the chemical conformation of RKs with improved hydrophilicity and deformability, which is pivotal for maintaining structural stability.[34,35] In this case, RKNFs met the long-term implantation requirements after SCI.

Biomaterial scaffolds have been widely used for the regeneration of nerve tissue. Emerging studies have shown that functional biomaterial scaffolds, such as collagen, silk, and chitosan, provide a supportive platform that facilitates cell adherence, cell survival, and axon outgrowth in SCI models.[14,15,36–38] However, the pro-inflammatory microenvironment after SCI may affect the therapeutic effect, probably limiting the further clinical application of biomaterial.[39] Concerns have also been raised related to the potential immunogenicity of biomaterials, which may result in a complex host response and aggravate the inflammatory reaction.[8] However, loading with anti-inflammatory factors or encapsulating immune cells can avoid these immunogenic reactions and rebalance the pro-inflammatory microenvironment.[35,40,41] In the present study, RKNF33A provided persistent inflammatory resolution up to 8 wpi, demonstrating that the implantation of RKNF33A bridging scaffold affected the microglia/macrophage response to pro-inflammatory stimuli and induced a sustained favorable pro-regenerative milieu. This study also showed a decreased cavity, increased myelin sparring and nerve regeneration, and ameliorated locomotor function in the RKNF33A group, proving that RK33A is a promising regulated immune biomaterial for scaffold fabrication after SCI.

The mechanism underlying RK33A-influenced M2 differentiation is not yet fully understood. During the heterologous expression, RKs were found in inclusion bodies, indicating the presence of massive disulfide bonds and poor solubility.[26] In the present study, RKs were directly added to the culture medium during in vitro experiments, whereas they were electrospun as bridging scaffolds during in vivo experiments. In both cases, RK33A presented a consistent and obvious immunomodulatory effect on M2 polarization. We speculate that RK33A is most likely to elicit an effect through a receptor-mediated process rather than via phagocytosis of soluble signals. Human hair keratins have been shown to contain the cell adhesion sequences Leu–Asp–Val (LDV) and Arg–Gly–Asp (EDS), which are known to support cellular recognition and attachment.[17] However, RK33A did not acquire these sequences, suggesting that there are other bioactive segments of trichocytic keratins leading to M2 microglia/macrophage polarization. Therefore, further studies are required to understand the relationship between the structural domains of trichocytic keratins and microglia/macrophage polarization.

Recent studies suggest that the PI3K/AKT/mTOR axis plays an important role in the M2 polarization of microglia/macrophages.[42,43] As previously reported, the phosphorylation of PI3K determines the induction of Arg1 (cytokine of M2 microglia/macrophage) and the activation of M2 microglia/macrophages.[44] AKT, the downstream target of PI3K, likely controls microglia/macrophage activation through multiple downstream effectors. AKT phosphorylation activates mTOR, contributing to its anti-inflammatory effects and apoptosis inhibition.[45,46] After suppressing mTOR by rapamycin, M2 microglia/macrophage tend to undergo apoptosis, while M1 microglia/macrophages secrete more inflammatory cytokines.[47] Consistent with previous studies,[48] our data showed that LPS inhibited the PI3K/AKT/mTOR pathway by downregulating the expression of PI3K, AKT, and mTOR, and this phenomenon could be reversed by RK33A addition. Previous studies have shown that integrin β1 or β3 play an important role in the cell recognition of keratins, and blockage of either integrin β1 or β3 receptors inhibits cell adhesion to keratin materials.[49] Additionally, integrin β1 has been reported to mediate the activation of PI3K/AKT.[50,51] In summary, we assumed that RK33A might promote M2 polarization of microglia/macrophages through an integrin-mediated process and, at least partially, by activating the PI3K/AKT/mTOR signaling pathway.

In this study, RK33A alone was sufficient for M2 phenotype microglia/macrophage switch and repair after SCI. However, the dilemma of spinal cord therapy can be attributed to the complicated pathophysiology of SCI, including the limited capacity for neuronal regeneration in the central nervous system, the generation of adverse factors, such as inflammatory cytokines and myelin decomposition products, and the lack of information to reconnect the synaptic interaction.[8,16,52] In this scenario, the combination of removing growth inhibitory factors, permissive trophic support, and transplantation of stem cells might have a superior effect in overcoming the barriers to nerve regeneration.[5] RK33A can be used as a scaffold construction material to combine multiple wound repair strategies after SCI. For example, cell transplantation strategies, including adult mesenchymal stem cell transplantation, have been shown to ameliorate anatomical and functional loss in animal models of SCI by promoting tissue sparing.[53] However, in the early stage post-SCI, the inflammatory events mentioned above usually generate a hostile microenvironment and therefore create obstacles for transplantation-oriented therapies.[5] In this case, RK33A used as a composite scaffold could provide a suitable immune environment for the transplanted loaded cells, offering cell attachment and migration cues for regenerated neural tissues simultaneously.

4. Conclusion

In this study, to our knowledge, 17 subtypes of keratin were screened for microglial polarization for the first time. Our results demonstrate that RK33A has a great effect on shifting microglia from M1 to M2 phenotype. Implantation of RKNF33A was beneficial in alleviating inflammation, reducing glial scar formation, and improving nerve regeneration, thereby promoting locomotor function recovery in the rat T9 hemisection model. We found that RK33A may achieve M2 microglia/macrophage polarization, at least partially, through the PI3K/AKT/mTOR signaling pathway. Collectively, RK33A has a significant immunomodulatory effect on M2 microglia/macrophage

ADVANCED
SCIENCE NEWS

www.advancedsciencenews.com

ADVANCED
FUNCTIONAL
MATERIALS

www.afm-journal.de

polarization, and as an implantable scaffold, favors neuroprotection and neuroregeneration after SCI.

5. Experimental Section

RKs Expression and Purification: All 17 RKs were expressed and purified as previously described with some modifications.[25] Gene sequences of different RKs were synthesized, cloned into pET-28a (+), and transformed into *E. coli* BL21 (DE3) for expression. Transformed *E. coli* cells were grown in the Luria–Bertani medium containing 50 µg mL^{-1} kanamycin at 37 °C. Once the optical density 600 reached 0.6–0.8, 1 mM isopropyl-β-D-thiogalactoside was added to induce the expression of cloned proteins at 37 °C for 4 h. Cells were subsequently harvested by centrifugation at 8000 rpm for 5 min at 4 °C. The precipitates (pellets) were dissolved in buffer A (50 mM Tris pH 8.0, 150 mM NaCl, 5 mM ethylenediaminetetraacetic acid [EDTA], and 20 mM β-mercaptoethanol), lysed twice using a high-pressure homogenizer (FB-110, Litu Machinery Equipment Engineering Co., Ltd. China) at 700 bar, and then centrifuged at 10 000 rpm for 20 min at 4 °C. Obtained pellets were sequentially resuspended in buffer B (buffer A containing, 1 M urea and 0.5% Triton-X-100), buffer C (50 mM Tris pH 8.0, 2.5 mM NaCl, 5 mM EDTA, 20 mM β-mercaptoethanol), and distilled water and centrifuged at 10 000 rpm for 20 min at 4 °C. Subsequently, the precipitates were completely dissolved in buffer D (50 mM Tris pH 8.0, 150 mM NaCl, 8 M urea, and 20 mM β-mercaptoethanol) and incubated with Ni-column resin (Ni Smart Beads 6FF, Changzhou Tiandi Renhe Biotechnology Co., Ltd. China) for 3 h at 4 °C in the vertical mixer. The beads were rinsed three times using ddH$_2$O to remove the impurities. The target proteins were eluted by adding 500 mM imidazole in buffer D. Eluted proteins were dialyzed (molecular weight cutoff of 10 kDa) against ddH$_2$O for 2 d for desalting. Finally, the protein solutions were lyophilized and sterilized with 60 Co γ-irradiation at a dose of 25 kGy.

Characterization of RKs: Purified RKs were mixed with 5X SDS-PAGE loading buffer and incubated for 10 min at 100 °C to denature the proteins. Electrophoretic separation was performed on a 10% SDS-polyacrylamide gel at 110 V for 90 min. After electrophoresis, the gels were stained using Coomassie Brilliant Blue for 30 min and subsequently destained twice using a destaining solution (Beyotime, China).

CD analysis of purified RKs was performed using a CD spectrophotometer (Chirascan, Applied Photophysics, UK) at room temperature. After subtracting the background spectra, protein spectra were obtained from 190 to 260 nm at a rate of 100 nm min^{-1}.

The chemical structures of purified RKs were determined using an FT-IR spectrometer (Nicolet 5DX, USA) in the wavenumber range of 500–4000 cm^{-1}. Purified RKs (in the form of powder) were blended with potassium bromide at a ratio of 1:100 and compressed into thin slices for testing.

BV2 Cell Culture and Treatment: BV2 microglial cells (kindly provided by Procell Life Science & Technology Co., Ltd.) were cultured in dulbecco's modified eagle medium (Gibco) supplemented with 10% fetal bovine serum and 1% streptomycin/penicillin (Gibco) in a humidified atmosphere containing 5% CO$_2$ at 37 °C. The medium was changed once a day, and the cells were passaged every two days. When the cells reached ≈60% confluence, they were incubated with LPS (100 ng mL^{-1}) and IFN-γ (20 ng mL^{-1}) with or without different RKs (200 µg mL^{-1}) for 24, 48, and 72 h. Finally, the cells were harvested for further experiments.

Cell Cytotoxicity Assay: Cytotoxicity of RKs was evaluated using the CCK-8 cell proliferation and cytotoxicity assay kit (Solarbio). After 24 and 48 h of incubation with different RKs in 96-well plates, BV2 cells were rinsed three times with phosphate-buffered saline (PBS), and 10 µL CCK-8 (prepared in fresh culture medium) was added to wells and incubated for 2 h at 37 °C. The optical absorbance of each sample was measured at 450 nm using a microplate reader (ELx808, BioTek Instruments, Inc., USA). The activity of RKs was calculated considering the activity of untreated cells as 100%.

Cytotoxicity of RKs was also assessed using the LIVE/DEAD viability/cytotoxicity assay kit (YEASEN Biotechnology, Shanghai, China) after 72 h of incubation with different RKs in 96-well plates. Treated BV2 cells were double-stained with calcein-acetoxymethyl and ethidium homodimer-1 to analyze cell viability (green) and cell death (red). Images of each well were captured using a fluorescence microscope (XDS-2FL, Optika, Italy).

Quantitative RT-PCR (qRT-PCR): LPS-stimulated BV2 cells (after treatment with different RKs for 24 h) were employed to extract total RNA using TRIzol (Invitrogen) according to the manufacturer's instructions, and subsequently, cDNA was synthesized using PrimeScript RT Master Mix (Takara). qPCR was performed using TB Green (Takara). The relative mRNA expression of genes was calculated and analyzed using the 2$-\Delta\Delta$Ct method, and the housekeeping gene GAPDH was used for normalization. Table S2 (Supporting Information) lists the primer sequences used for the target genes.

Flow Cytometry Analysis: After LPS stimulation with or without RK83, RK35, or RK333A for 24 h, BV2 cells were washed twice with PBS, and a single-cell suspension containing 2% bovine serum albumin (BSA) was prepared. Suspensions were incubated with antibodies (PE-CD86 [Proteintech, PE-65068, 1:100] and APC-CD206 [Elabscience, E-AB-F1135E, 1:100]) at 4 °C in darkness for 1 h. Cells were harvested by centrifugation at 2000 rpm for 5 min and washed twice with PBS to remove unbound antibodies. Finally, the suspension was analyzed using flow cytometry (BD Influx).

Western Blotting: After treatment with or without LPS and RK33A for 24 h, BV2 cells were lysed using radioimmunoprecipitation assay buffer containing 1% phenylmethylsulfonyl fluoride. After separation using 10% SDS-PAGE gels, cellular proteins were transferred electrophoretically onto polyvinylidene difluoride membranes and blocked in 5% BSA in Tris-buffered saline with 0.05% Tween-20. Membranes were incubated with primary antibodies overnight at 4 °C, washed, and then incubated for 2 h at room temperature with a secondary antibody. ECL substrate (Advansta, USA) was used for chemiluminescence-based detection of protein bands, and the density of protein bands was quantified using ImageJ software (Wayne Rasband and contributors National Institutes of Health, USA). Antibodies against p-mTOR (Proteintech, 80596-1-RR, 1:1000), mTOR (proteintech,28273-1-AP, 1:1000), p-PI3K (SAB, 11 508, 1:1000), PI3K (Proteintech, 60225-1-lg), p-AKT (SAB, 13 357), AKT (Proteintech, 60203-2-Ig, 1:1000), and β-actin (SAB, 48 139, 1:2000) were used. Appropriate secondary antibodies were purchased from Beyotime and used at 1:500 dilution.

Fabrication of RKNFs: PCL nanofibers and RKNFs were prepared using electrospinning. PCL, with or without RKs (8/2 w/w), was dissolved in hexafluoroisopropanol at a final concentration of 10 wt% w/v. The solution was loaded into a 5 mL syringe, which was then attached to a syringe pump (Baoding Langer, China). The positive electrode of the electrostatic generator was connected to the needle (21G), and the negative electrode was connected to a drum collector covered with aluminum foil. Electrospinning was carried out at a rotating speed of 1000 rpm, voltage of 15 kV, a flow rate of 1.5 mL h^{-1}, and receiving distance of 20–25 cm at room temperature to create aligned nanofibers. Each nanofiber was detached from the aluminum foil and rolled along the longitudinal direction of nanofiber orientation to form a cylindrical scaffold. The nanofibers were sterilized using 60 Co γ-irradiation at a dose of 25 kGy and kept dried for further animal experiments.

Characterization of RKNFs: The morphologies of the PCL nanofibers and RKNFs were observed using SEM (Nova 400, FEI, USA) at an accelerating voltage of 5.0 kV. The samples were tailored into 5 × 5 mm^2 slices, coated with gold for 15 s, and observed under SEM. The fiber diameters were determined using SEM images and further analyzed using the ImageJ software.

The structural combinations of PCL and RKs in RKNFs were characterized using an FT-IR spectrometer (Nicolet 5DX, USA), as previously described.

The hydrophilicity of the PCL nanofibers and RKNFs was determined by water contact angle measurements using a contact angle meter (XG-CAMA, Xuan Standard Instrument. China). Distilled water was dropped onto the surface of the nanofibers, and the shape of the droplet

**ADVANCED
SCIENCE NEWS**

www.advancedsciencenews.com

**ADVANCED
FUNCTIONAL
MATERIALS**

www.afm-journal.de

was captured immediately. The contact angles were calculated from the slopes of the curves using ImageJ software.

The mechanical properties of the PCL nanofibers and RKNFs were measured using a universal testing machine (CTM2100, Xie Qiang Instrument Manufacturing Co., ltd) working with a load cell of 500 N and a displacement speed of 30 mm min^{-1} until failure. The thicknesses of the samples were measured using a digital Vernier caliper. The tensile strength and elongation were calculated from the generated data.

SCI Animal Experiments: The rat T9 spinal cord lateral hemisection model was used to evaluate nerve regeneration.[54] The animal experiments were approved by the Animal Care and Use Committee of Chongqing Medical University (2022-K535). Thirty-six-week-old female Sprague Dawley (SD) rats (200 ± 20 g) purchased from the Experimental Animal Center of Chongqing Medical University (Chongqing, China) were divided into five groups according to the nanofiber composite (SCI, PCL, RKNF83, RKNF35, and RKNF33A groups).

The rats were anesthetized by intraperitoneal injection of pentobarbital (30 mg kg^{-1}). Hairs over the thoracic vertebrae were shaved, and the surgical area was cleaned three times using iodophor and ethanol. A midline skin incision (3 cm) was made on the back over T8–11. Under a surgical microscope, the paraspinal muscles were bluntly separated and retracted from the surgical area, exposing the spinous process and vertebral plate. The T9 spinous process was cautiously snipped away, and the upper lamina was removed using a rongeur. The midline was identified by inserting a needle (30 G) vertically through the midline into the spinal cord, with the beveled side facing the right side under a surgical microscope. The right side of the spinal cord was removed to create a 2 mm coloboma. Bleeding was stopped using sterile hemostatic sponges. Subsequently, the cylindrical scaffold (2 × 2 × 2 mm), either PCL nanofibers or RKNF, was implanted into the defect area, allowing the orientation of nanofibers to be consistent with the long axis of the spinal cord. The muscle and skin layers were sutured separately. After surgery, each rat was injected with 0.9% sterile saline subcutaneously to maintain hydration, and buprenorphine (2.0 mg kg^{-1}) twice a day subcutaneously for 2 d to ease the pain. Each rat received manual bladder extrusion twice daily until reflexive bladder control was restored.

Animal Motor Function Evaluation: Hind limb recovery was assessed by two blinded scorers using the BBB locomotor score behavioral assessment at 1, 3 d, 1, 2, 3, 4, and 8 weeks post-injury. The BBB score ranges from 0 (completely paralyzed) to 21 (normal functional recovery) based on the observation of hind limb movements during free movements of rats.

Footprint analysis was performed in a homemade alley (80 × 40 cm) floored with white paper at 4 and 8 wpi. The rats' fore and hind paws were marked in red and blue, respectively. The rats were then placed at one end of the alley and allowed to pass straight to the other end. Footprints were captured using a Sony RX1 camera. Stride length (the distance between the center pads of the forelimbs and hindlimbs) was measured using ImageJ to assess limb coordination ability.

The open-field test was performed in a homemade square field (80 × 80 × 40 cm) in a dark space. At 4 and 8 wpi, the rats were allowed 2 min to familiarize themselves with the environment and 5 min to move freely in the field. The animal tracker plugin in ImageJ was used to track the walking path in the field. The silence was maintained during the test to avoid the influence of sound on the experimental results, and 75% alcohol was used to completely clean the field after each test to avoid the influence of residual smell.

Tissue Paraffin Sections Preparation: At 1 and 8 wpi, three rats in each group were randomly sacrificed and perfused with cooled (4 °C) normal saline and 4% paraformaldehyde successively through ventriculus sinister. The 2 cm spinal cord tissue at the lesion site was removed and fixed in PFA overnight. The fixed spinal cord tissue was embedded in paraffin, cut longitudinally to 4 μm thickness, and stored at room temperature until further processing.

HE and LFB Staining: After deparaffinization and rehydration, HE and LFB staining were performed according to the manufacturer's instructions (Solarbio). The sections were examined under an optical microscope.

Immunofluorescence Staining: BV2 cells were fixed with 4% PFA and deparaffinized, and rehydrated spinal cord tissues were permeabilized with 0.5% Triton X-100 for 15 min and blocked with 5% BSA for 1 h. Fixed cells and tissues were incubated with primary antibodies at 4 °C overnight. After three PBS containing 0.05% Tween-20 washes, samples were incubated with secondary antibodies for 1 h at room temperature, and nuclei were stained with DAPI (Beyotime, China). Fluorescent images were captured using a fluorescence microscope (XDS-2FL; Optika, Italy). The following antibodies were used: CD86 (Zenbio, 501199, 1:200), CD206 (proteintech, 60143-1-Ig, 1:200), GFAP (CST, #3670, 1:500), NF200 (proteintech, 18934-1-AP, 1:500), β-tubulin III (proteintech, 66375-1-Ig, 1:500), and Iba-1 (Abcam, ab178846, 1:500). Appropriate secondary antibodies were purchased from Beyotime and used at 1:500 dilution.

ELISA: The levels of proinflammatory cytokines (TNF-α) and anti-inflammatory cytokines (IL-10) in the serum of rats were measured using ELISA kits (MEIMIAN, CHINA) at 1 and 8 wpi. The assays were performed according to the manufacturer's protocol. Absorbance at 450 nm was recorded using a microplate reader (ELx808, BioTek Instruments, Inc., USA).

Statistical Analysis: All data are expressed as the mean ± standard error of the mean. Comparisons among groups were performed using one- or two-way analysis of variance with a post hoc Tukey's multiple comparison test. All analyses were conducted using GraphPad Prism 8.0 and Origin 2021 software. All tests were two-sided, and the statistical significance was set at $p < 0.05$.

Supporting Information

Supporting Information is available from the Wiley Online Library or from the author.

Conflict of Interest

The authors declare no conflict of interest.

Data Availability Statement

Research data are not shared.

[1] T. H. Hutson, S. Di Giovanni, *Nat. Rev. Neurol.* **2019**, *15*, 732.

[2] C. S. Ahuja, J. R. Wilson, S. Nori, M. R. N. Kotter, C. Druschel, A. Curt, M. G. Fehlings, *Nat. Rev. Dis. Primers* **2017**, *3*, 17018.

[3] C. S. Ahuja, M. Fehlings, *Stem Cells Transl. Med.* **2016**, *5*, 914.

[4] D. J. Hellenbrand, C. M. Quinn, Z. J. Piper, C. N. Morehouse, J. A. Fixel, A. S. Hanna, *J. Neuroinflammation* **2021**, *18*, 284.

[5] I. Vismara, S. Papa, F. Rossi, G. Forloni, P. Veglianese, *Trends Mol. Med.* **2017**, *23*, 831.

[6] S. David, A. Kroner, *Nat. Rev. Neurosci.* **2011**, *12*, 388.

[7] L. M. Milich, C. B. Ryan, J. K. Lee, *Acta Neuropathol.* **2019**, *137*, 785.

[8] T. Führmann, P. N. Anandakumaran, M. S. Shoichet, *Adv. Healthcare Mater.* **2017**, *6*, 1601130.

[9] G. Courtine, M. V. Sofroniew, *Nat. Med.* **2019**, *25*, 898.

[10] A. Hurtado, J. M. Cregg, H. B. Wang, D. F. Wendell, M. Oudega, R. J. Gilbert, J. W. McDonald, *Biomaterials* **2011**, *32*, 6068.

[11] K. Zhang, H. Zheng, S. Liang, C. Gao, *Acta Biomater.* **2016**, *37*, 131.

[12] H. Xia, Q. Chen, Y. Fang, D. Liu, D. Zhong, H. Wu, Y. Xia, Y. Yan, W. Tang, X. Sun, *Brain Res.* **2014**, *1565*, 18.

[13] H. Xia, Y. Xia, *Mater. Sci. Eng. C* **2018**, *91*, 228.

[14] Y. Zou, D. Ma, H. Shen, Y. Zhao, B. Xu, Y. Fan, Z. Sun, B. Chen, W. Xue, Y. Shi, Z. Xiao, R. Gu, J. Dai, *Biomater. Sci.* **2020**, *8*, 5145.

[15] J. Chedly, S. Soares, A. Montembault, Y. von Boxberg, M. Veron-Ravaille, C. Mouffle, M.-N. Benassy, J. Taxi, L. David, F. Nothias, *Biomaterials* **2017**, *138*, 91.

[16] T. M. O'Shea, J. E. Burda, M. V. Sofroniew, *J. Clin. Invest.* **2017**, *127*, 3259.

[17] J. G. Rouse, M. E. Van Dyke, *Materials* **2010**, *3*, 999.

[18] Z. Cheng, R. Qing, S. Hao, Y. Ding, H. Yin, G. Zha, X. Chen, J. Ji, B. Wang, *Regener. Biomater.* **2021**, *8*, rbab008.

[19] S. Reichl, *Biomaterials* **2009**, *30*, 6854.

[20] T. Luo, S. Hao, X. Chen, J. Wang, Q. Yang, Y. Wang, Y. Weng, H. Wei, J. Zhou, B. Wang, *Mater. Sci. Eng. C* **2016**, *63*, 352.

[21] Y. He, Q. Qu, T. Luo, Y. Gong, Z. Hou, J. Deng, Y. Xu, B. Wang, S. Hao, *ACS Biomater. Sci. Eng.* **2019**, *5*, 1113.

[22] X. Chen, D. Zhai, B. Wang, S. Hao, J. Song, Z. Peng, *J. Mater. Sci.* **2020**, *31*, 28.

[23] B. V. Fearing, M. E. Van Dyke, *Acta Biomater.* **2014**, *10*, 3136.

[24] M. Waters, P. VandeVord, M. Van Dyke, *Acta Biomater.* **2018**, *66*, 213.

[25] F. Gao, W. Li, J. Deng, J. Kan, T. Guo, B. Wang, S. Hao, *ACS Appl. Mater. Interfaces* **2019**, *11*, 18681.

[26] J. Kan, W. Li, R. Qing, F. Gao, Y. Wang, L. Zhu, B. Wang, S. Hao, *Chem. Mater.* **2020**, *32*, 3122.

[27] S. Nallamsetty, D. S. Waugh, *Nat. Protoc.* **2007**, *2*, 383.

[28] T. Guo, W. Li, J. Wang, T. Luo, D. Lou, B. Wang, S. Hao, *Artif. Cells Nanomed. Biotechnol.* **2018**, *46*, 456.

[29] K. Xi, Y. Gu, J. Tang, H. Chen, Y. Xu, L. Wu, F. Cai, L. Deng, H. Yang, Q. Shi, W. Cui, L. Chen, *Nat. Commun.* **2020**, *11*, 4504.

[30] S. Tavakol, S. M. M. Mousavi, B. Tavakol, E. Hoveizi, J. Ai, S. M. R. Sorkhabadi, *Mol. Neurobiol.* **2017**, *54*, 2483.

[31] M. Xue, V. W. Yong, *Lancet Neurol.* **2020**, *19*, 1023.

[32] M. Hagen, J. A. Sembill, M. I. Sprügel, S. T. Gerner, D. Madžar, H. Lücking, P. Hölter, S. Schwab, H. B. Huttner, J. B. Kuramatsu, *Neurol.–Neuroimmunol. Neuroinflamm.* **2019**, *6*, 588.

[33] V. B. Risbrough, M. N. Vaughn, S. F. Friend, *Biol. Psychiatry* **2022**, *91*, 438.

[34] M. Rampichová, J. Chvojka, M. Buzgo, E. Prosecká, P. Mikeš, L. Vysloužilová, D. Tvrdík, P. Kochová, T. Gregor, D. Lukáš, E. Amler, *Cell Proliferation* **2013**, *46*, 23.

[35] X. Sun, C. Zhang, J. Xu, H. Zhai, S. Liu, Y. Xu, Y. Hu, H. Long, Y. Bai, D. Quan, *ACS Biomater. Sci. Eng.* **2020**, *6*, 1228.

[36] Q. Zhang, B. Shi, J. Ding, L. Yan, J. P. Thawani, C. Fu, X. Chen, *Acta Biomater.* **2019**, *88*, 57.

[37] A. Marchini, A. Raspa, R. Pugliese, M. A. El Malek, V. Pastori, M. Lecchi, A. L. Vescovi, F. Gelain, *Proc. Natl. Acad. Sci. USA* **2019**, *116*, 7483.

[38] X. Gao, W. Cheng, X. Zhang, Z. Zhou, Z. Ding, X. Zhou, Q. Lu, D. L. Kaplan, *ACS Appl. Mater. Interfaces* **2022**, *14*, 3701.

[39] D. Ma, Y. Zhao, L. Huang, Z. Xiao, B. Chen, Y. Shi, H. Shen, J. Dai, *Biomaterials* **2020**, *237*, 119830.

[40] S. Chen, S. Liu, L. Zhang, Q. Han, H. Liu, J. Shen, G. Li, L. Zhang, Y. Yang, *Chem. Eng. J.* **2020**, *399*, 125795.

[41] G. Li, M. T. Che, K. Zhang, L. N. Qin, Y. T. Zhang, R. Q. Chen, L. M. Rong, S. Liu, Y. Ding, H. Y. Shen, S. M. Long, J. L. Wu, E. A. Ling, Y. S. Zeng, *Biomaterials* **2016**, *83*, 233.

[42] X. He, Y. Li, B. Deng, A. Lin, G. Zhang, M. Ma, Y. Wang, Y. Yang, X. Kang, *Cell Proliferation* **2022**, *55*, e13275.

[43] H. Y. Zhao, Y. Y. Zhang, T. Xing, S. Q. Tang, Q. Wen, Z. S. Lyu, M. Lv, Y. Wang, L. P. Xu, X. H. Zhang, Y. Kong, X. J. Huang, *Signal Transduction Targeted Ther.* **2021**, *6*, 234.

[44] S. B. Weisser, K. W. McLarren, N. Voglmaier, C. J. van Netten-Thomas, A. Antov, R. A. Flavell, L. M. Sly, *Eur. J. Immunol.* **2011**, *41*, 1742.

[45] A. J. Covarrubias, H. I. Aksoylar, T. Horng, *Semin. Immunol.* **2015**, *27*, 286.

[46] P. Liu, H. Cheng, T. M. Roberts, J. J. Zhao, *Nat. Rev. Drug Discovery* **2009**, *8*, 627.

[47] A. Mercalli, I. Calavita, E. Dugnani, A. Citro, E. Cantarelli, R. Nano, R. Melzi, P. Maffi, A. Secchi, V. Sordi, L. Piemonti, *Immunol.* **2013**, *140*, 179.

[48] M. Xue, W. Sheng, X. Song, Y. Shi, Z. Geng, L. Shen, R. Wang, H. Lü, J. Hu, *CNS Neurosci. Ther.* **2022**, *28*, 1059.

[49] L. R. Burnett, M. B. Rahmany, J. R. Richter, T. A. Aboushwareb, D. Eberli, C. L. Ward, G. Orlando, R. R. Hantgan, M. E. Van Dyke, *Biomaterials* **2013**, *34*, 2632.

[50] R. Izmailyan, J.-C. Hsao, C.-S. Chung, C.-H. Chen, P. W.-C. Hsu, C.-L. Liao, W. Chang, *J. Virol.* **2012**, *86*, 6677.

[51] M. A. Riquelme, S. Gu, R. Hua, J. X. Jiang, *Bone Res.* **2021**, *9*, 8.

[52] J. W. Squair, M. Gautier, M. V. Sofroniew, G. Courtine, M. A. Anderson, *Curr. Opin. Biotechnol.* **2021**, *72*, 48.

[53] D. Joung, V. Truong, C. C. Neitzke, S.-Z. Guo, P. J. Walsh, J. R. Monat, F. Meng, S. H. Park, J. R. Dutton, A. M. Parr, M. C. McAlpine, *Adv. Funct. Mater.* **2018**, *28*, 1801850.

[54] C. Chen, J. Tang, Y. Gu, L. Liu, X. Liu, L. Deng, C. Martins, B. Sarmento, W. Cui, L. Chen, *Adv. Funct. Mater.* **2019**, *29*, 1806899.